RSC Advances

PAPER

View Article Online
View Journal | View Issue

Cite this: *RSC Adv.*, 2024, **14**, 18536

Preparation and characterization of Fe–ZnO cellulose-based nanofiber mats with self-sterilizing photocatalytic activity to enhance antibacterial applications under visible light†

Kithmini Ranathunga,‡[a] Piumika Yapa, ‡[a] Imalka Munaweera, *[a] M. M. Weerasekera [b] and Chanaka Sandaruwan [cd]

Bacterial infections and antibiotic resistance have posed a severe threat to public health in recent years. One emerging and promising approach to this issue is the photocatalytic sterilization of nanohybrids. By utilizing ZnO photocatalytic sterilization, the drawbacks of conventional antibacterial treatments can be efficiently addressed. This study examines the enhanced photocatalytic sterilizing effectiveness of Fe-doped ZnO nanoparticles (Fe–ZnO nanohybrids) incorporated into polymer membranes that are active in visible light. Using the co-precipitation procedure, Fe–ZnO nanohybrids ($Fe_xZn_{100-x}O$) have been generated using a range of dopant ratios (x = 0, 3, 5, 7, and 10) and characterized. The ability to scavenge free radicals was assessed and the IC_{50} value was calculated using the DPPH test at different catalytic concentrations. PXRD patterns showed a hexagonal wurtzite structure, which indicated that the particle size of the nanohybrid decreased as the dopant concentration rose. It was demonstrated by UV-vis diffuse reflectance experiments that the band gap of the nanohybrid decreased (redshifted) with Fe doping. The photocatalytic activity under sunlight increased steadily to 87% after Fe was added as a dopant. The Fe 5%–ZnO nanohybrid exhibited the lowest IC_{50} value of 81.44 μg mL^{-1} compared to ZnO, indicating the highest radical scavenging activity and the best antimicrobial activity. The Fe 5%–ZnO nanohybrid, which is proven to have the best photocatalytic sterilization activity, was then incorporated into a cellulose acetate polymer membrane by electrospinning. Disc diffusion assay confirmed the highest antimicrobial activity of the Fe 5%–ZnO nanohybrid incorporated electrospun membrane against *Staphylococcus aureus* (ATCC 25923), *Streptococcus pneumoniae* (ATCC 49619), *Escherichia coli* (ATCC 25922), *Pseudomonas aeruginosa* (ATCC 27853), and *Candida albicans* (ATCC 10231) under visible light. As a result, Fe 5%–ZnO nanofiber membranes have the potential to be employed as self-sterilizing materials in healthcare settings.

Received 27th April 2024
Accepted 4th June 2024

DOI: 10.1039/d4ra03136a

rsc.li/rsc-advances

1 Introduction

Nanotechnology has transformed numerous disciplines across a wide range of fields in recent decades. Its nanoscale size enables it to have better features, which have helped it reach several important milestones in biomedical applications. Nanoparticle-based materials show exceptional properties when utilized as medicinal agents, particularly for conditions that do not respond well to conventional treatments.[1–3] Sterilization is the process of permanently inactivating or eliminating all live microorganisms and their spores.[4] Self-sterilizing materials possess a distinctive ability to reduce the quantity of interacting microorganisms by causing redox stress and destroying the microorganisms by photothermal or photocatalytic mechanisms.[5] To maintain public health standards, there is currently a demand for sustainable polymeric materials with an antibacterial capability for biomedical applications such as personal protection equipment (PPE), medical gowns, bedclothes, and other medical textiles that are utilized in hospitals.[6,7]

Despite their extensive use, conventional sterilization procedures like UV irradiation, ozonation, and chlorination have a number of drawbacks, including photo corrosion, low visible light utilization, and the formation of carcinogenic byproducts.[8–10] The biomedical field has expanded its boundaries with the introduction of the photocatalytic sterilization procedure, a developing approach that uses a light source to

[a]Department of Chemistry, Faculty of Applied Sciences, University of Sri Jayewardenepura, Nugegoda, Sri Lanka. E-mail: imalka@sjp.ac.lk
[b]Department of Microbiology, Faculty of Medical Sciences, University of Sri Jayewardenepura, Nugegoda, Sri Lanka
[c]Sri Lanka Institute of Nanotechnology (SLINTEC), Homagama, Sri Lanka
[d]Department of Aerospace Engineering, Khalifa University of Science and Technology, 127788, Abu Dhabi, United Arab Emirates

† Electronic supplementary information (ESI) available. See DOI: https://doi.org/10.1039/d4ra03136a

‡ Equally contributed.

accelerate the sterilization process. Once light radiation is captured by the photocatalyst, photoinduced electrons and holes are produced, and these particles move to the surface of the catalysts.[11,12] Superoxide radicals are produced when adsorbed oxygen interacts with electrons. Furthermore, adsorbed water molecules or surface hydroxyl groups absorb holes, resulting in the formation of reactive oxygen species (ROS) known as hydroxyl radicals ($OH^{\bullet}$). The hydroxyl radical is the most potent oxidant capable of inactivating bacteria. As a result, ROS fuel the photocatalytic sterilization process.[13–15]

ROS reduces microbial cells' antioxidant-dependent defense system by oxidizing lipids and organelles such as proteins and DNA. Most microorganisms produce an acidic environment in their host cells, thus catalysts breakdown in biological fluids as a result of this increased acidity. The increasing acidity then enhances the production of hydroxyl groups. This causes bacterial cells to run out of glutathione and produce more reactive oxygen species (ROS), which have a number of negative impacts on the microbial cells.[16,17]

In terms of microbiological illnesses, numerous examples of contamination and pollution have occurred around the world in recent years, posing a major threat to human health. As is generally known, the number of bacterial strains demonstrating antibiotic resistance is increasing annually, and some of these types are extremely difficult to eliminate.[18] Since the beginning of the twentieth century, pathogens have consistently succeeded to avoid the effects of antimicrobial medications.[19,20] According to the information provided above, photocatalytic sterilization has sparked significant interest since it offers a promising way for removing pathogenic germs. Furthermore, successful photocatalytic sterilization requires the discovery of a novel photocatalyst with excellent absorption across a wide range of wavelengths as well as surface durability.

Advances have been made in the production of antimicrobial photocatalysts, including natural compounds, antibiotics, and nanoparticles, for sterilization purposes.[21–25] The discovery of metal nanoparticles and their potential for therapeutic applications ushered in a new chapter of biomedicine.[26] Scientists from all over the world have been astounded by the powerful antibacterial qualities they have demonstrated against a variety of microorganisms. In response to the multiple issues that have emerged, the scientific arena has refocused its efforts on the hunt for novel antimicrobial compounds.[27,28]

Zinc oxide (ZnO) is a non-hazardous and thermodynamically stable inorganic metal oxide.[29] However, it is less effective in visible light because to its huge band gap energy ($E_g = 3.37$ eV) and high exciton binding energy (60 mV). Thus, high-energy UV radiation is required to start the photocatalytic sterilization process. When sunlight is used as an energy source, pure ZnO demonstrates inadequate photocatalytic properties since sunlight only contains 2–3% UV radiation and 47% visible light, making it low energetic and renewable.[30] Its absorption spectrum must thus be significantly broadened from ultraviolet to visible light. Several notable changes to ZnO have been established, including the doping of metal or nonmetal and the generation of heterojunction semiconductors.[31] Doping is the process of introducing foreign components into a pure substance in order to modify its new properties. Dopants create a new band between the valence and conduction bands, reducing the band gap significantly. The remarkable link between the structural, optical, and magnetic properties of ZnO doped with Cr, Mn, and Fe has generated renewed interest. It is critical to select acceptable ionic radii for dopants. Fe^{3+} has an ionic radius of 64 pm, and Zn^{2+} has an ionic radius of 74 pm. Doping with varied Fe^{3+} concentrations improve electron hole pair separation while also decreasing average particle size.[32–34]

Owing to its three-dimensional porous framework, highly effective expanse of surface, and adaptability in operation, the electrospun nanofiber has been believed to be the best possible candidate to immobilize the photocatalyst on an appropriate solid inert substrate that possesses the envisioned morphological structure.[35] A simple, well-developed technique called electrospinning uses electrostatic forces to fabricate ultrathin fibers with nanoscale dimensions. Electrospinning produces membranes with a larger surface area to volume ratio than membranes made using other techniques. Furthermore, due to their fibrous structure, which makes it more difficult to detach the powdered catalysts from the reaction mixture, the electrospun nanofiber membrane ensures that the photocatalysts are reusable. Consequently, an efficient way to address the catalyst recovery issue would be to develop electrospun nanofiber incorporated with photocatalyst.[36,37]

Considering the recent published research, Qi *et al.* has developed Mn, Co, Ni, and Cu doped ZnO and has proved that Cu doped ZnO nanoparticles possess the best antimicrobial activity among other nanohybrids, especially against *E. coli*.[38] Moreover, Guo *et al.* also developed Ta doped ZnO nanoparticles and have proved that it has an antibacterial activity against many Gram-positive and Gram-negative bacteria.[39] Permyakova *et al.* have developed ZnO-modified polycaprolactone nanofibers (PCL-ZnO) by treating the nanofiber surface with plasma in a gaseous mixture of $Ar/CO_2/C_2H_4$ followed by the deposition of ZnO nanoparticles with both antibacterial and antifungal activity.[40] Similarly, Sekar *et al.* have studied a prominent bactericidal activity of nanofibers and was detected with the increase in Fe-doped ZnO nanoparticles (NPs) concentration against Gram-positive *Staphylococcus aureus* and Gram-negative *Escherichia coli*.[41] With those successful stories, the purpose of this research was to create and evaluate visible light active Fe–ZnO nanoparticles combined into an electrospun membrane with the potential to be employed as a self-sterilizing material. Fe–ZnO nanohybrids ($Fe_xZn_{100-x}O$) were synthesized using the co-precipitation process and used as a photocatalyst. The synthesis technique was resumed with different dopant ratios ($x = 0$, 3, 5, 7, and 10) and characterized. ZnO is a well-proven photocatalyst that has antibacterial properties. The photocatalytic activity of the nanoparticles was determined using a methylene blue dye degradation test. The ability to scavenge free radicals was evaluated using the DPPH assay at various catalytic concentrations, and an IC_{50} value was derived. The synthesized Fe–ZnO nanohybrids were then electrospun into a suitable polymer membrane. Fig. 1 depicts an illustration that describes the research outline.

Finally, the antibacterial activity of the produced membrane was evaluated, demonstrating that this novel electrospun

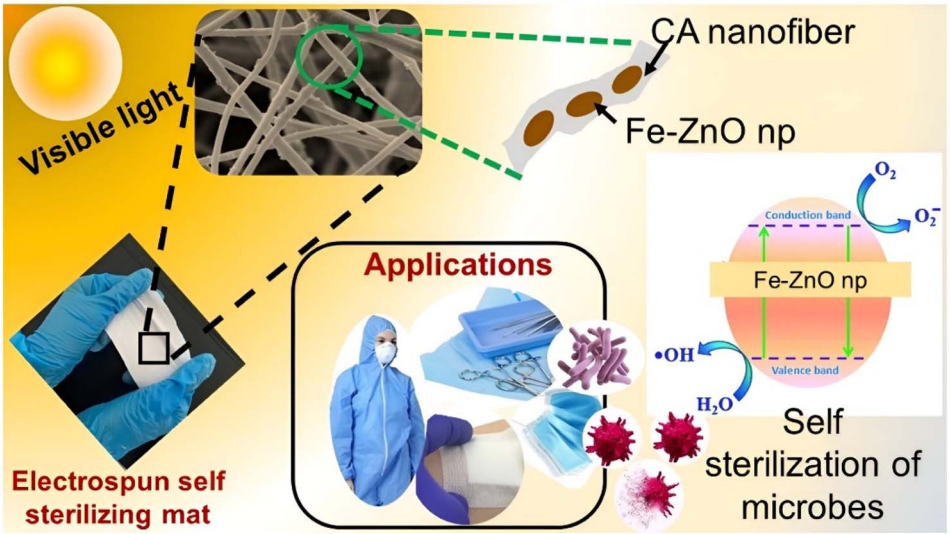

Fig. 1 An illustration of the research overview.

membrane with Fe–ZnO nanohybrids can be exploited as a possible self-sterilizing photocatalytic membrane in biomedical applications. It is a low-cost, biodegradable, and environmentally friendly solution for recovering, reusing, and recycling photocatalyst. Furthermore, using visible light for photocatalysis ensures the free use of complex photocatalytic technology in this circumstance. To our knowledge, this is the first work to focus on the self-sterilizing photocatalytic characteristics of cellulose acetate based polymeric Fe–ZnO nanofiber membranes.

2 Materials and methods

2.1 Materials and reagents

All reagents, metal precursors, and other chemicals, including zinc acetate dihydrate, ferric chloride, sodium hydroxide (NaOH), polyethyleneglycol 6000 (PEG_{6000}), methylene blue, 2,2 diphenyl-1-picrylhydrazyl (DPPH), methanol, ascorbic acid, acetone, dimethylformamide, cellulose acetate, sodium chloride (NaCl), barium chloride ($BaCl_2$), and sulfuric acid (H_2SO_4) were obtained from Sigma Aldrich, USA. Chemicals, media, and other materials for microbiology research, such as nutritional agar, Muller Hinton agar, Muller Hinton broth agar, bacteriological agar, blood agar, and antibiotic powders were obtained from HiMedia in India. All compounds used were in analytical grade. ATCC strains of *Staphylococcus aureus* (ATCC 25923), *Streptococcus pneumoniae* (ATCC 49619), *Escherichia coli* (ATCC 25922), *Pseudomonas aeruginosa* (ATCC 27853), and *Candida albicans* (ATCC 10231) were obtained from the Department of Microbiology, University of Sri Jayewardenepura, Sri Lanka.

2.2 Synthesis and characterization of ZnO and Fe–ZnO nanoparticles

Exactly, 3.38 g of zinc acetate dihydrate was dissolved in 50 mL of deionized water. PEG_{6000} was added to that solution followed by the dropwise addition of 2 M NaOH. The reaction mixture was stirred for 2 hours, and the resultant gel was centrifuged and washed with deionized water three times. The resultant precipitate was then oven dried at 100 °C for 12 hours. The oven dried product was calcined at 450 °C for 2 hours to obtain zinc oxide nanoparticles. To obtain the fine powder of ZnO nanoparticles, the calcined ZnO nanoparticles were further ground using mortar and pestle.[42]

Zinc acetate dihydrate solution was prepared by dissolving 4.278 g of zinc acetate in 50 mL of deionized water. A ferric chloride solution was prepared by mixing 0.1655 g of ferric chloride in 30 mL of deionized water. Both solutions were mixed at once. PEG_{6000} was added to that solution followed by the dropwise addition of 2 M NaOH. The reaction mixture was stirred for 2 hours, the resultant gel was centrifuged and washed with deionized water three times. The precipitates were collected, and oven dried at 100 °C for 12 hours. The oven dried product was calcinated at 450 °C for 2 hours to obtain Fe 5%–ZnO nanohybrid. The aforementioned procedure was followed to obtain Fe 3%–ZnO, Fe 7%–ZnO and Fe 10%–ZnO nanohybrids using 0.0993 g, 0.2317 g, and 0.3310 g ferric chloride, respectively.[43,44]

The crystalline structures of synthesized nanohybrids were investigated by powder X-ray diffraction (PXRD) analysis (Rigaku smart lab, 3 kW sealed X-ray tube, CBO optics, D/teX Ultra 250 silicon strip detector) within the range of 7–80 two theta degrees. In order to study the functional groups, present in the compound along with the inter molecular interactions, the synthesized nanohybrids were subjected to Fourier transform infrared (FTIR) analysis – KBr pellet method (Bruker Vertex 80 instrument) within the range (400 to 4000 cm^{-1}). The optical band gaps of synthesized nanohybrids were evaluated by UV-vis diffuse reflectance (PerkinElmer instrument, UV Express – version 4.1.3) within the range of 300 to 800 nm. The morphological characteristics of synthesized nanohybrids were studied by scanning electron microscopy (SEM) imaging (ZEISS model, mode of secondary electron, at an accelerating voltage of

10 kV). To analyze the elemental composition of samples, X-ray photoelectron spectroscopic (XPS) analysis (Thermo Scientific TM ESCALAB Xi+ apparatus) was carried out.[45]

2.3 Evaluation of the photocatalytic activity of nanohybrids

The photocatalytic activity of pure ZnO and Fe–ZnO nanohybrids was determined by observing the degradation of a methylene blue dye solution. About 2 mg of methylene blue was taken into a 500 mL volumetric flask and it was topped up with distilled water. Then 15 mL of prepared methylene blue solution and 20 mg of catalyst were mixed, and the samples were kept in the dark for 1 hour to reach the adsorption desorption equilibrium. A photodegradation experiment was carried out under sunlight (intensity 45–75 kLux) and under visible light lamp (50 W LED) while continuously stirring the solutions using magnetic stirrer for 1 hour. After every 15 minutes time interval, aliquots (5 mL) were extracted and centrifuged. To measure the photocatalytic degradation over time, UV-vis spectra were taken in the range of 300–800 nm and the monitoring wavelength of methylene blue at 663 nm was used.[46]

2.4 Evaluation of the antimicrobial activity of synthesized nanohybrid powders followed by the photocatalytic activation

ZnO and Fe–ZnO nanohybrids were tested against the ATCC cultures of Gram-positive bacteria; *Staphylococcus aureus* (ATCC 25923), *Streptococcus pneumoniae* (ATCC 49619), Gram-negative bacteria; *Escherichia coli* (ATCC 25922), *Pseudomonas aeruginosa* (ATCC 27853) and fungi; *Candida albicans* (ATCC 10231). These microorganisms are predominant pathogenic microbes which can be commonly observed in humans. Commercially available antibiotics; erythromycin (100 μg) was used as the positive control for Gram-positive bacteria. Gentamycin (100 μg) was used for Gram-negative bacteria and fluconazole (100 μg) was used for *Candida albicans*.

The prepared media (Muller Hinton Agar for *S. aureus*, *E. coli* and *P. aeruginosa*, blood agar for *S. pneumoniae* and Sabouraud Dextrose Agar for *C. albicans*) and tips of the micropipette were sterilized in an autoclave at 121 °C (15 bar pressure) for 15 minutes. Other glass ware was sterilized in a hot air oven at 160 °C for 2 hours. A quantity of 25 mL of Muller Hinton agar was poured into each disposable Petri dish and allowed to solidify. Then suspensions of all the selected microorganisms were prepared, which were adjusted with their concentrations to, 0.5 McFarland's standard (10^8 CFU mL^{-1}) and then followed by a serial dilution until the final concentration reached to 10^{-4} CFU mL^{-1}. Afterwards, 3 mL of each suspension were placed in centrifuge tubes. These tubes were labelled as; positive control (standard antibiotic 100 μg), negative control (microbial suspension), Fe–ZnO nanohybrids in sunlight, normal light, lamp, and dark.

Then the tube which was labeled as ZnO. Fe in sunlight, normal light, lamp, and dark were exposed to sunlight, normal light, lamp (50 W warm white LED with wavelength range of 400 to 700 nm) and dark for 2 hours after adding Fe (5%)–ZnO nanohybrid to it. All these tubes were coupled with a negative control and a positive control before the exposure. Then 100 μL from each tube were pipetted out and cultured on the solidified agar plates. All the agar plates were incubated for 24 hours at 37 °C. Finally, the colony count was counted by the quadrant method. The percentage reduction in microbial growth was calculated using the formula below.[47–49]

$$\text{Percentage bacterial growth reduction}(\%) = \frac{\frac{\text{CFU}}{\text{mL}}\text{Negative control} - \frac{\text{CFU}}{\text{mL}}\text{Sample}}{\frac{\text{CFU}}{\text{mL}}\text{Negative control}} \times 100\%$$

The best formulation for Fe–ZnO nanohybrid was chosen based on the antibacterial activity of synthesized nanohybrid powders, that were subsequently photocatalytically activated.

2.5 Determination of radical scavenging activity and IC_{50} values of ZnO and Fe 5%–ZnO nanohybrids by DPPH assay

The free radical scavenging activity of nanohybrids were measured using the 2,2 diphenyl-1-picrylhydrazyl (DPPH) assay method and the IC_{50} value was calculated. Exactly 1 mL of 100 μM DPPH prepared in methanol was added to 1 mL of nanohybrid solution prepared at different concentrations by dispersing it in distilled water. Ascorbic acid (0.1 M) was used as the standard. Absorbance was recorded at 517 nm and DPPH scavenging activity was calculated with the following equation.

$$\text{DPPH scavenging activity} = \frac{A_0 - A_1}{A_0} \times 100\%$$

where A_0 and A_1 are absorbance of DPPH and sample respectively.[50,51]

2.6 Fabrication and characterization of nanohybrids incorporated electrospun cellulose acetate (CA) nanofibers

For the preparation of polymer solution about 600 mg of cellulose acetate (100 kDa) was taken into a glass vial and then acetone: DMF were added in a 2 : 1 v/v ratio, which means 4 mL of acetone and 2 mL of DMF were mixed in the glass vial. It was then stirred for 1 hour at ambient room temperature and humidity and 180 mg of Fe 5%–ZnO nanohybrid was added to the mixture in order to fabricate the 30% (w/w) loaded CA nanofiber mat. Then the solution was stirred for about 6 hours to ensure the homogeneous dispersion of the nanohybrid in the polymer solution. Then the solution was sonicated for about 30 minutes. Afterwards, the solution was loaded into a syringe attached to a blunt end needle. Then an aluminium foil was spread on the ground collector to collect fibers. The solution was electrospinning using 16 kV voltage, a 13 cm tip to collector distance, and a 1.5 mL h^{-1} flow rate to produce the CA nanofiber mat, ZnO nanoparticles incorporated the CA mat and Fe 5%–ZnO nanohybrid incorporated the CA nanofiber mat[52] using SKE EF100 electrospinning system with a static collector plate at ambient room temperature and humidity.

The crystalline structures of synthesized nanofibers were studied by PXRD analysis within the range of 7–80 two theta degrees. In order to analyze the functional groups, FTIR analysis was carried out in ATR mode within the range of 525–

4000 cm^{-1}. The morphological characteristics of nanofiber membranes were studied using SEM imaging. The content of Fe in the Fe 5%–ZnO nanohybrid incorporated electrospun membrane was analyzed using the AAS analysis. A manual digestion method by an acid mixture was performed prior to this analysis. A square shaped sample of 100 cm^2 was taken from the electrospun CA membrane. Then 1 cm^2 sample from middle and each corner of the 100 cm^2 portion of the mat were taken and added to boiling tubes separately and three samples from each corner and middle were taken to triplicate the experiment. In a fume hood a mixture of conc. HCl and conc. HNO_3 in a ratio of 3 : 1 was added to the sample and then the mixture was boiled gently over a water bath at 95 °C for 4–5 hours until the sample had completely dissolved. These solutions were subjected to AAS analysis.[53]

2.7 Evaluation of the photocatalytic activity and determination of free radical scavenging activity of ZnO nanoparticles and Fe 5%–ZnO nanohybrid incorporated CA electrospun nanofiber membranes

The photocatalytic activity of ZnO incorporated cellulose acetate fiber mat and Fe 5%–ZnO nanohybrid incorporated CA fiber mats were determined by analyzing the degradation of a methylene blue dye solution. A 1 cm^2 portion of the mat was taken from each sample and mixed with 15 mL of prepared methylene blue (MB) solution separately. The samples were kept in the dark for 1 hour to reach the adsorption desorption equilibrium prior to the analysis. Then the photodegradation experiment was carried out under normal light and a visible light lamp (50 W LED) while continuously stirring the MB solutions using magnetic stirrer for 1 hour. After every 15 minutes time interval, MB aliquots (5 mL) were extracted and centrifuged. To measure the photocatalytic degradation over time, UV-vis spectra of MB samples were taken in the range of 300–800 nm and the peak at 663 nm wavelength of methylene blue was considered for the analysis.[54]

In order to determine the free radical scavenging activity of the fabricated nanofiber membranes, DPPH test was carried out. A 0.5 cm^2 portion of a membrane was taken to a test tube, and 1 mL of distilled water and 1 mL of DPPH were added. The mixture was shaken well, and after 30 minutes, absorbance was measured at 517 nm. The percentage of DPPH degradation was calculated with the following equation. The analysis was triplicated using separate portions of the fiber membranes.

$$\text{DPPH scavenging activity} = \frac{A_0 - A_1}{A_0} \times 100\%$$

where A_0 and A_1 are absorbance of DPPH and sample respectively.

2.8 Evaluation of the antimicrobial activity of ZnO nanoparticles and Fe 5%–ZnO nanohybrid incorporated electrospun CA membranes

The disc diffusion method was conducted to observe the antibacterial activity of the ZnO and Fe 5%–ZnO nanohybrid incorporated electrospun polymer membranes. ZnO and Fe 5%–ZnO nanohybrid incorporated electrospun membranes were tested against the ATCC cultures of Gram-positive bacteria; *Staphylococcus aureus* (ATCC 25923), *Streptococcus pneumoniae* (ATCC 49619), Gram-negative bacteria; *Escherichia coli* (ATCC 25922), *Pseudomonas aeruginosa* (ATCC 27853), and fungi *Candida albicans* (ATCC 10231). These microorganisms are pathogenic microbes which cause infections in humans. Commercially available antibiotic discs of erythromycin (15 μg) were used as the positive control for Gram-positive bacteria. Gentamycin (10 μg) was used for Gram negative bacteria, and fluconazole (15 μg) was used for *Candida albicans*. Cellulose acetate electrospun membrane was used as the negative control. The diameter of the discs that were used for the assays was 6 mm.[55,56]

As mentioned in the Section 2.4, the media was prepared, autoclaved, bacterial suspensions were prepared and cultured in prepared plates. The excess microbial suspension was then carefully removed by using a micropipette. The bacterial suspensions were prepared by using fresh cultures of the aforementioned bacteria. Discs were placed on the surface of the solidified agar by using sterile forceps, and then all the plates were incubated for 24 hours at 37 °C. Afterwards, the zone of inhibition for each well was measured (Netillin Zone Reader, USA). All the procedures were triplicated and conducted according to the CLSI guidelines.[45,46,57]

3 Results and discussion

The synthesis technique of the photocatalytic nanomaterial in this study is primarily concerned with simplicity, cost-effectiveness, and biocompatibility, while also improving self-sterilization activity. For this aim, photocatalytic ZnO and Fe–ZnO nanohybrids were synthesized utilizing the co-precipitation approach, which is cost-effective, easily reproducible, easy, and gives a greater yield while preserving outstanding purity. Additionally, it yields materials with a controlled particle dimensions,[58,59] uniform dispersion, expansion, and adjustability in comparison to alternative synthesis methods. The ZnO photocatalyst is modified by doping the substance with Fe^{3+}. The photocatalytic investigation then explores the optimal doping ratio by using methylene blue degradation to examine the most effective photocatalyst under visible light conditions. Fe 5%–ZnO nanohybrid exhibited the best photocatalytic activity accordingly, and then they were incorporated into a biopolymer matrix (cellulose acetate) by using the technique of electrospinning. The Fe 5%–ZnO nanohybrid incorporated electrospun membrane was then proven for its antimicrobial activity. Hence, the final product of this research is a biodegradable, affordable, biocompatible, accessible, and effective photocatalyst incorporated polymer membrane, which was proven for its self-sterilization properties and possesses the ability to readily be used in health care settings.

3.1 Characterization of the synthesized ZnO and Fe–ZnO nanohybrids

Initially, structural and morphological characterization were performed in order to confirm the successful synthesis of ZnO

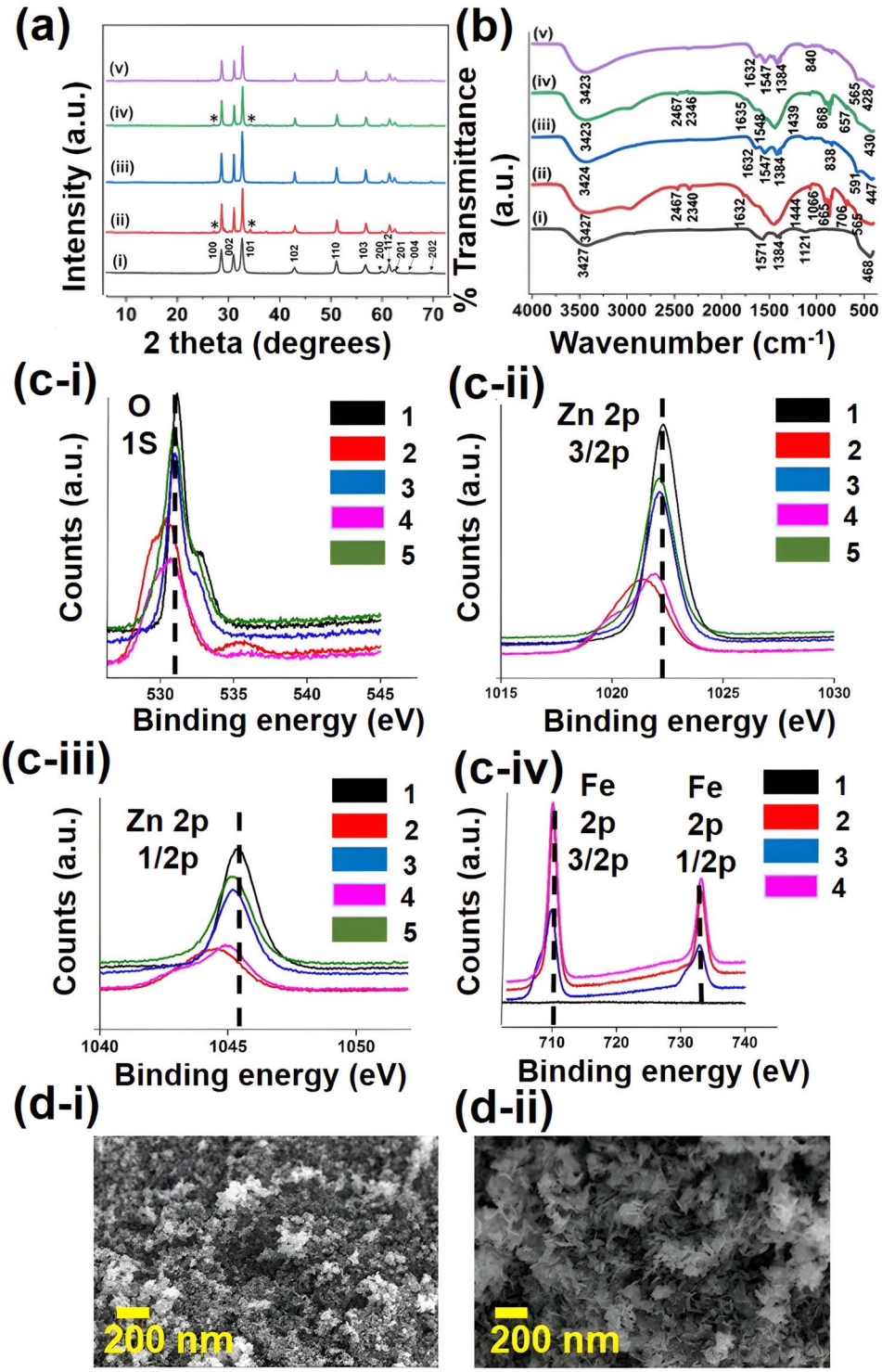

Fig. 2 (a) PXRD spectra of synthesized nanohybrids; (b) FTIR spectra of synthesized nanohybrids; (i) ZnO, (ii) Fe 3%–ZnO, (iii) Fe 5%–ZnO, (iv) Fe 7%–ZnO and (v) Fe 10%–ZnO; (c) binding energy differences of; (c-(i)) O 1s state, (c-(ii)) Zn $2p_{3/2}$ state, (c-(iii)) Zn $2p_{1/2}$ state, (1) ZnO, (2) Fe 3%–ZnO, (3) Fe 5%–ZnO, (4) Fe 7%–ZnO and (5) Fe 10%–ZnO; (c-(iv)) binding energy differences of Fe; (1) Fe 3%–ZnO, (2) Fe 5%–ZnO, (3) Fe 7%–ZnO and (4) Fe 10%–ZnO; (d-(i)) SEM image of ZnO and (d-(ii)) SEM image of Fe 5%–ZnO.

and Fe–ZnO nanohybrids. The PXRD analysis was performed to analyze the crystalline phases of each nanohybrid. The PXRD patterns of pure ZnO and Fe–ZnO nanocrystalline samples with different dopant ratios (x = 0, 0.03, 0.05, 0.07, and 0.10) are shown in Fig. 2a. The observed diffraction peaks of samples have been compared with the JCPDS file no. 36-1451 of ZnO, which confirms the wurtzite phase of ZnO that was present in all the analyzed samples. Moreover, the sharp peaks denote the crystalline nature of the prepared samples. The lattice planes of (100), (002), (101), (102), (110), (103), (200), (112), (201), (004),

and (202) in the X-ray diffractograms were identified, and these peaks governed the ZnO crystalline phases. In the samples of ZnO and Fe 5%–ZnO nanohybrid, no additional peak apart from that corresponding to ZnO was detected. In the samples of Fe 3%–ZnO nanohybrid and Fe 7%–ZnO nanohybrid, additional peaks were observed which is corresponding to secondary phases of $ZnFe_2O_4$.[60] These peaks which are responsible for impurities are denoted by an asterisk (*) in the Fig. 2a. The concentration of the dopant can significantly affect the crystalline structures of the nanomaterials. At lower concentrations, the dopant atoms may incorporate into the ZnO lattice less uniformly, leading to formation of impurity phases. At higher concentrations, clustering or segregation of dopant atoms may occur, resulting impurity phases.[61]

The findings of the PXRD study revealed that the values of lattice constants (a and c) and average crystalline size dropped as the Fe doping percentage increased. These differences in lattice parameters could be attributed to the substitutional replacement of Fe^{3+} ions in place of Zn^{2+} ionic sites in the ZnO matrix, resulting in a minor misfit due to the varying ionic radius of Fe^{3+} ions *versus* Zn^{2+} ions. This was also supported by reducing the unit cell volume of ZnO from 47.62 $(A°)^3$ to 47.43 $(A°)^3$ while increasing the Fe content from 0% to 10%. Table 1 displays the crystalline size and lattice characteristics of pure ZnO nanoparticles and Fe–ZnO nanohybrids[29]

The formation of the ZnO structure in the synthesized nanohybrids were further supported by FTIR analysis, as shown in Fig. 2b. The functional groups, peak positions, and relevant peak shifts of the nanohybrids were identified with FTIR analysis. The metal–oxygen bonds usually appear in the fingerprint region, and they are clearly shown in the spectrum as evidence of successful doping of Fe into the ZnO matrix. The broad band that appears around 3425 cm^{-1} is related to the O–H stretching vibration of adsorbed water molecules. The weak band that appears around 2360 cm^{-1} is mainly due to CO adsorption on the surface from the CO_2 in the atmosphere. The band located around 1635 cm^{-1} is due to the H–O–H bending vibration of water in ZnO. The peak at 1547 cm^{-1} is assigned to the C–H bending mode. The peak around 1384 cm^{-1} is due to the C=O asymmetric stretching vibration of residual carboxylate on the surface. The band, which is located around 1121 cm^{-1} is due to the C–O single bond stretching mode. Bands with an intensity of medium to weak, at 839 cm^{-1} to 669 cm^{-1} are assigned to vibrational frequencies due to the changes in microstructural features caused by the doping of Fe into the ZnO lattice.

The peak that is located around 565 cm^{-1} to 660 cm^{-1} is due to the Fe–O stretching mode. The band that is presented around 468 cm^{-1} can be assigned to the Zn–O stretching mode, which also confirms the formation of the ZnO wurtzite structure,[53] and that band has shifted to the right slightly by causing a red shift, as a result of the incorporation of Fe^{3+} into ZnO lattice.[62,63]

XPS analysis was carried out to further identify the chemical composition, oxidation sate, and electronic configuration of the pure ZnO and Fe–ZnO nanohybrids, as depicted in Fig. 2c(i–iv). The peaks with a high intensity that is observed at 1022.28 eV and 1042.32 eV binding energies, respectively, correspond to Zn $2p_{3/2}$ and Zn $2p_{1/2}$ states (Fig. 2c(ii and iii)). The observed binding energies of these peaks are different from the elemental binding energy values and close to the standard binding energy values of 'Zn' in ZnO. This indicates that zinc is present in +2 chemical states in the analyzed samples.[64]

The binding energies of Zn $2p_{3/2}$ are located at 1022.28, 1021.40, 1022.10, 1021.85, and 1022.02 eV for 0%, 3%, 5%, 7%, and 10% Fe–ZnO samples, respectively. The binding energy of central Zn $2p_{3/2}$ shows asymmetrical behavior for Fe–ZnO samples. In the Zn 2p spectra of Fe–ZnO in Fig. 2c(ii and iii), two Zn 2p bands have been shifted slightly, denoting that Fe has been successfully doped into the ZnO matrix.

The O 1s peak observed at 531.16 eV is due to lattice oxygen bonded with Zn atoms (Fig. 2c(i)). The binding energies of O 1s are located at 531.16, 530.38, 530.97, 530.67, and 530.92 eV for 0%, 3%, 5%, 7%, and 10% Fe–ZnO samples, respectively. The broad nature of the peak could be due to various coordination of oxygen in the films. As reported in the literature, the O 1s peak can be fitted into three Gaussian peaks having different binding energy positions. Among these three peaks, the peak on the lower binding energy side is attributed to the O^{2-} ions in the wurtzite structure of hexagonal ZnO. Fig. 2c(iv) shows the binding energy differences of Fe $2p_{1/2}$ and $2p_{3/2}$ states in 3%, 5%, 7% and 10% Fe–ZnO samples. The intensity of the peaks grew as the proportion of Fe doped into the ZnO matrix increased. Furthermore, the binding energies of Fe $2p_{1/2}$ and $2p_{3/2}$ states increased as the doping fraction was raised.[65,66]

The optical band gap energy (E_g) of the Fe–ZnO samples was then determined using UV-vis diffuse reflectance spectroscopy. The optical band gap energy of a material can be determined by measuring the absorption corresponding to the transition from the valence band to the conduction band. The graphs of $(F(R)\,h\nu)^2$ *versus* $h\nu$ for pure ZnO nanoparticles and Fe–ZnO nanohybrids were recorded. The band gaps of each sample were

Table 1 Average crystallite size and lattice parameters of pure ZnO nanoparticles and Fe–ZnO nanohybrids

Compound	Average crystallite size (nm)	Unit cell parameters (Å) $a = b$	Unit cell parameters (Å) c	Volume $(Å)^3$
Pure ZnO np	26.21	3.25	5.21	47.62
Fe 3%–ZnO nanohybrid	36.84	3.25	5.20	47.55
Fe 5%–ZnO nanohybrid	32.03	3.25	5.21	47.59
Fe 7%–ZnO nanohybrid	31.80	3.24	5.19	46.33
Fe 10%–ZnO nanohybrid	30.63	3.25	5.19	47.43

Table 2 Band gap energies of pure ZnO nanoparticles and Fe doped ZnO nanohybrid

Compound name	Band gap energy (eV)	Wavelength (nm)
ZnO np	3.37	368
Fe 3%–ZnO nanohybrid	3.29	377
Fe 5%–ZnO nanohybrid	3.09	402
Fe 7%–ZnO nanohybrid	3.27	379
Fe 10%–ZnO nanohybrid	3.87	320

determined by extrapolating the linear portion of the plot to the $(F(R)h\nu)^2 = 0$ axis (ESI File 01†). The direct band gap of undoped ZnO is found to be 3.37 eV. It almost matches the band gap value of ZnO reported in the literature.[67] When doping Fe^{3+} into the ZnO lattice, the band gap values have decreased. Estimated band gap values for all samples show a red shift with respect to the pure ZnO sample, except for Fe 10%–ZnO, which exhibits a blue shift. It is reported that the cause of red-shift in the band gap values may be due to strong sp–d exchange interactions.[68] These exchange interactions arise between the band electrons of ZnO and the localized d electrons of Fe atoms when Fe ions substitute some of the Zn ions in ZnO. When the dopant level was raised from 0 to 5%, the band gap energy was reduced from 3.37 eV to 3.09 eV. The band gap values obtained for each sample are in Table 2.[68]

After revealing that the Fe 5%–ZnO nanohybrid exhibit the lowest band gap energy, the morphological characteristics of ZnO and Fe 5%–ZnO nanohybrid were studied by SEM, as shown in Fig. 2d(i and ii). The morphology of the samples has changed from nanospheres to nanoflowers with the doping of Fe because the dopant atoms might affect the particle size and can change crystal growth directions in various directions. In ZnO, usually the *c* axis conveys the greatest growth rate, but upon the addition of dopant, it generates a thermodynamic barrier that slows down both the nucleation and the growth rate in primary nuclei. The concentration and rate of OH^- ions also affected the morphology because they were directed to anisotropic crystal growth.[69,70]

3.2 Evaluation of the photocatalytic activity of the synthesized nanohybrids

The photocatalytic activity of synthesized nanohybrids were evaluated by the degradation of Methylene Blue (MB) dye under different lighting conditions as illustrated by Fig. 3a–c. The

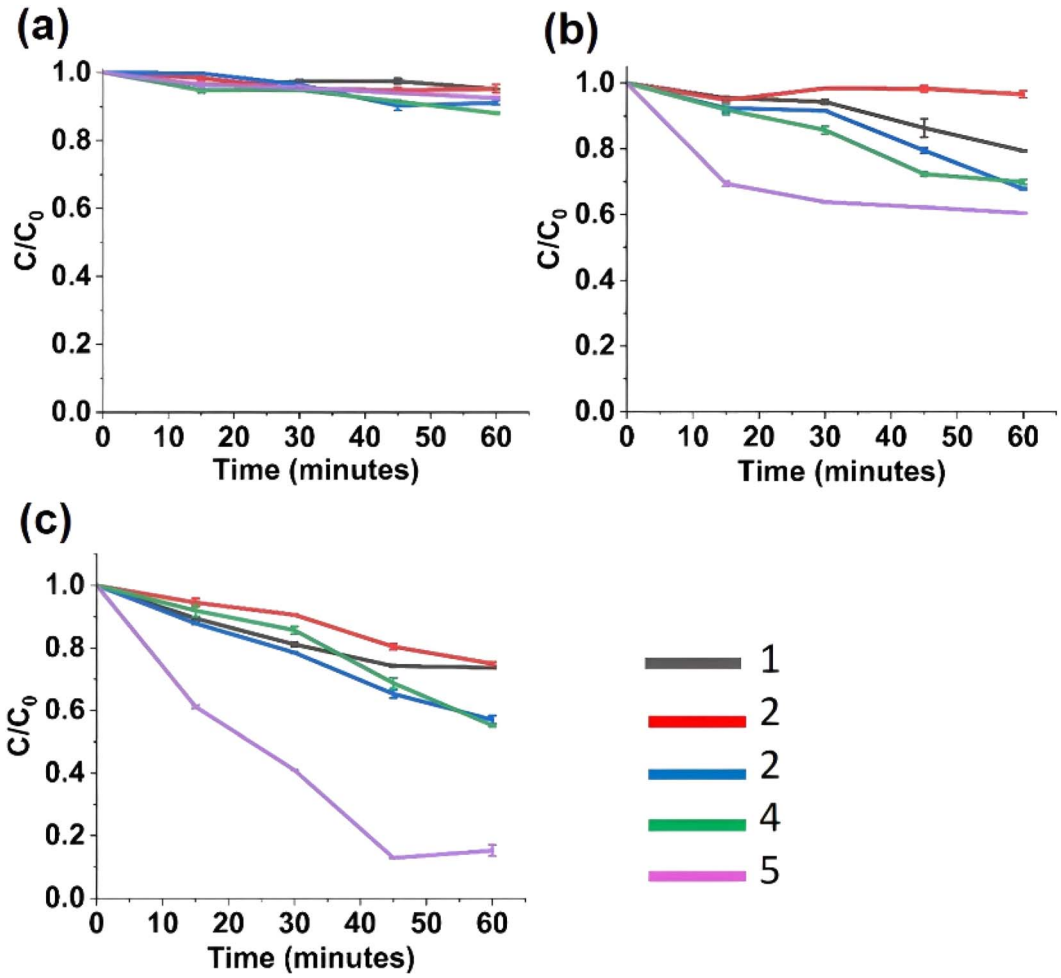

Fig. 3 Photocatalytic studies of nanohybrids under (a) under dark; (b) under visible light lamp; (c) under sunlight; (1) ZnO, (2) Fe 3%–ZnO, (3) Fe 5%–ZnO, (4) Fe 7%–ZnO, (5) Fe 10%–ZnO.

degradation of MB dye by the photocatalysts was monitored through the reduction of characteristic absorption peak height (ESI Fig. S2–S4†). The percentage of degradation of MB dye is defined as the measure of degradation efficiency of the photocatalyst.

The following is the mechanism involved in the photocatalytic degradation of ZnO. First, the MB dye is adsorbed onto the ZnO nanostructures' catalytic surface. Then, when exposed to light from a lamp or sunshine, it causes excitons to form in ZnO. After reacting with the oxygen adsorbed on ZnO, the photogenerated electrons present in the conduction band of ZnO produce superoxide anion radicals ($O_2^{-\bullet}$). Similar to this, when hydroxyl groups on the surface react with the holes made in ZnO's valence band, extremely reactive hydroxyl radicals ($OH^{\bullet}$) are produced. Reactive radicals may also be produced by the dissociation of water molecules brought on by these photogenerated holes. When extremely reactive hydroxyl and superoxide radicals react with the MB dye adsorbed on ZnO, it degrades/decolorizes.

Fig. 3c shows the photocatalytic degradation of MB under sunlight. For a one-hour time period, Fe 5%–ZnO nanohybrid shows the highest degradation, and it was found to be 87% and for ZnO under sunlight (intensity 45–75 kLux), photocatalytic degradation was found to be 27%, and hence Fe 5%–ZnO nanohybrid shows a more promising efficiency in photocatalytic degradation than undoped ZnO. Also, Fe 3%–ZnO nanohybrid, and Fe 7%–ZnO nanohybrid showed higher photocatalytic degradation than undoped ZnO, which was found to be 42.9% and 44.82%, respectively. The reason for enhancing the photocatalytic activity of Fe 5%–ZnO nanohybrid, Fe 3%–ZnO nanohybrid and Fe 7%–ZnO nanohybrid the is broadening of the absorbed wavelength range of light with the enhanced photogenerated charge separation.[71]

3.3 Evaluation of IC_{50} value of the synthesized nanohybrids by DPPH assay

The free radical scavenging activity of ZnO particles in the presence of $DPPH^{\bullet}$ in the methanolic solution could be described by the generally accepted mechanism of semiconductor based photocatalysis. The mechanism involved the transformation of $DPPH^{\bullet}$ into DDPH upon the donation of electrons on the oxygen atoms to the odd electrons of the nitrogen atoms, resulting in the formation of stable DPPH molecules.

IC_{50} is the concentration at which 50% of the total DPPH free radical is scavenged or neutralized and can be determined by the linear regression method by plotting % inhibition against the corresponding concentration, as shown in Fig. 4a and b. Both ZnO and Fe 5%–ZnO nanohybrid show the radical scavenging activity and IC_{50} values were calculated as 106.6 μg mL^{-1} and 81.44 μg mL^{-1} for ZnO and Fe 5%–ZnO nanohybrid, respectively. It was observed that the IC_{50} value of Fe 5%–ZnO nanohybrid is less than that of ZnO. It happens because of the higher generation of free radicals in Fe 5%–ZnO nanohybrid due to its lower band gap energy. The lower value for IC_{50} is responsible for a higher radical scavenging activity. Hence, Fe 5%–ZnO nanohybrid, which exhibit the lowest IC_{50} value, possess the highest radical scavenging activity.[72,73]

3.4 Evaluation of the antimicrobial activity of the nanohybrids with the photocatalytic activation

Photocatalysis is an innovative green technique based on advanced oxidation process that produces various reactive substances, have gained greater attention for their promising application as conventional antimicrobial agents.[74] Photocatalysts are substances that alter the rate of a chemical reaction when they are exposed to light with the proper wavelength.[75] Here we have employed synthesized nanohybrids as the photocatalysts and they were evaluated for their photocatalytic activity in different conditions; sunlight, normal light, lamp, and dark.

The antimicrobial studies of ZnO and Fe 5%–ZnO nanohybrid are shown in Fig. 4b. In all the samples, the highest reduction rate was shown by samples which were kept under sunlight. The highest percentage reduction of growth was observed in *S. aureus* under sunlight. The second highest reduction rate was shown by samples that were kept under normal light, and the highest percentage reduction of growth was observed in *S. pneumoniae*. For the samples that were kept under a visible light lamp, there was no significant reduction in microbial growth except for *E. coli*.

After the characterization of synthesized nanohybrids, they were subjected to electrospinning in order to fabricate a photocatalyst that incorporates polymer membrane, which can be readily used as a self-sterilizing material. Considering the aforementioned data, the Fe 5%–ZnO nanohybrid was confirmed as the best photocatalyst among those synthesized nanohybrids, and it was used to fabricate the electrospun polymer membranes. ZnO incorporated electrospun membranes and cellulose acetate electrospun membranes were also fabricated and used as controls for comparative studies.[76,77]

3.5 Characterization of the fabricated ZnO nanoparticles and Fe 5%–ZnO nanohybrid incorporated electrospun CA membranes

XRD analysis was performed initially for cellulose acetate polymer (CA), CA with ZnO, and CA with Fe 5%–ZnO nanohybrid loaded nanofiber Fig. 5a membranes, as shown in Fig. 5b. The XRD patterns of all the samples exhibit the cellulose acetate peaks concerning cellulose amorphous type. Moreover, the incorporation of ZnO and Fe 5%–ZnO nanohybrid can be identified by the sharp peaks in the range of two theta 20–80. For fabricating Fe–ZnO nanofiber mats, Fe 5%–ZnO nanohybrid were used since they showed the best photocatalytic activity, as discussed above. The XRD patterns for lattice planes of (100), (002), (101), (102), (110), (103), (112), and (201) were identified as the predominant peaks in the Fe–ZnO incorporated CA membranes that govern the ZnO and Fe_2O_3 crystalline phases.

Afterwards, the FTIR spectra of electrospun nanofiber membranes were analyzed in ATR mode, as shown in Fig. 5c. The O–H stretching peak appears to be weak in the 3400–3500 cm^{-1} range. The peak usually occurs around 2900 cm^{-1} due to C–H stretching, which was not observed here. The vibration peak around 1700 cm^{-1} is attributed to the C=O stretching vibration.

Also, the peak around 1430 cm^{-1} was attributed to the $-CH_2-$ deformation vibration that occurred. Further, the characteristic

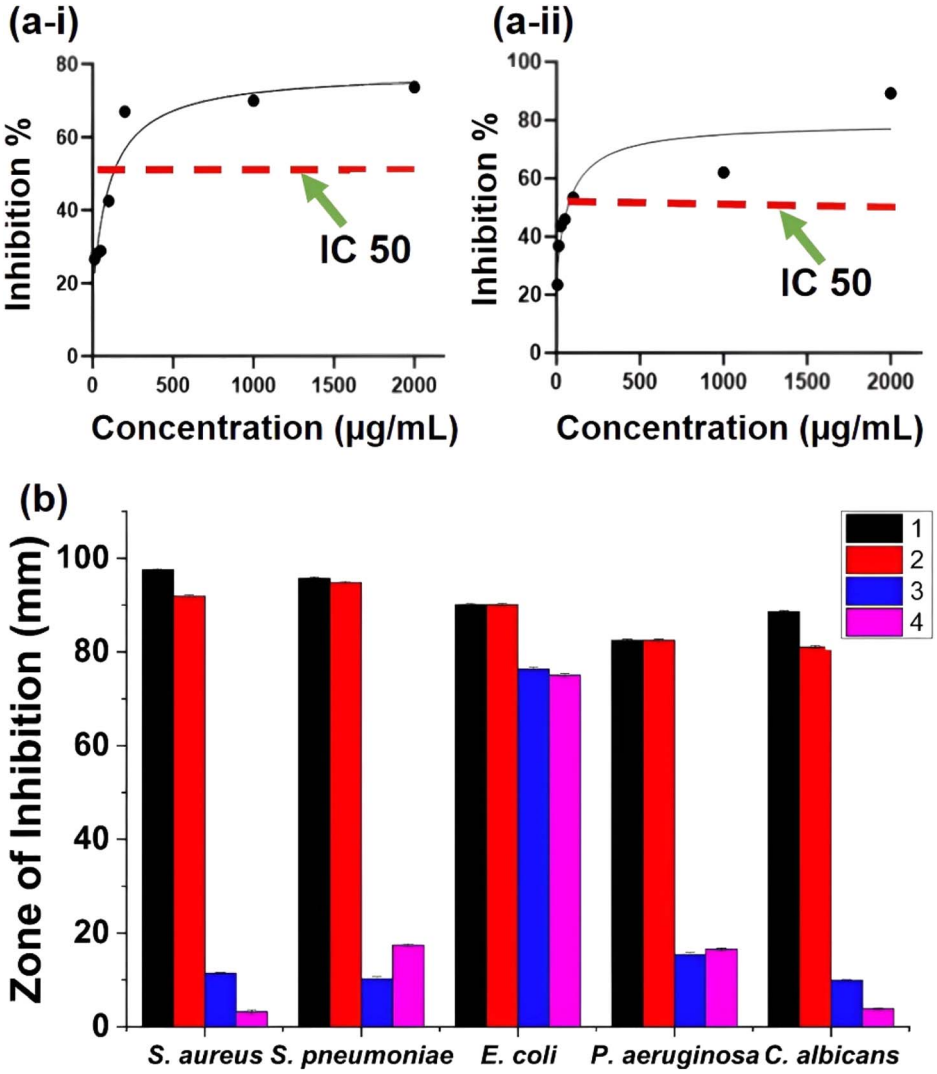

Fig. 4 (a) DPPH free radical scavenging activity of ZnO nanoparticles; (b) DPPH free radical scavenging activity of Fe 5%–ZnO nanoparticles; (c) percentage reduction of growth of different microorganisms in Fe 5%–ZnO nanohybrids kept under different conditions; (S= Sunlight, N=Normal light, L = Lamp, D = Dark), (1) Fe 5%–ZnO S, (2) Fe 5%–ZnO N, (3) Fe 5%–ZnO L and (4) Fe 5%–ZnO D.

peak at 1230 cm^{-1} was observed due to C–O carboxylate stretching vibrations. The peak at around 1039 cm^{-1} was observed due to the –C–OH stretching vibration. It is noted that the presence of the absorption peaks at around 900 cm^{-1} could be due to both –C–O stretching and $-CH_2$ rocking vibrations. In the fingerprint region, some peaks are observed in the range of 500–900 cm^{-1} which may be due to metal–O bonds. The peak position shift and the change in intensity of the peaks denote the incorporation of Fe–ZnO.[78,79]

The morphology of electrospun nanofibers were analyzed by SEM, as shown in Fig. 5d(i–iii). In CA nanofiber with ZnO and Fe 5%–ZnO nanohybrid, it can be seen that beads are formed along with the fiber that is normally considered to have defects. Also, it can be observed that fiber diameter has been reduced with the incorporation of nanohybrids. The addition of metal doped ZnO nanoparticles resulted in the accumulation of a higher charge density on the surface of the ejected jet during electrospinning, and the overall charges carried by the electrospinning jet significantly increased. As the charges carried by the jet increased, higher elongation forces that could overcome the self-repulsion were brought down to the jet under the electric field. Thus, as the charge density increased, the diameter of the fibers became smaller. The SEM images were then analyzed by the software ImageJ to obtain the mean diameter of the electrospun fibers and to investigate the distribution of fiber diameter (Fig. 5e(i–iii)). The mean diameters of the fibers were 121 ± 4, 89 ± 4 and 96 ± 4 nm that belong to CA electrospun membrane, the ZnO incorporated CA membrane, and Fe doped 5%-ZnO incorporated CA membrane, respectively.[80]

Then the fabricated mats were digested manually by a mixture of acids (HCl and conc. HNO_3 in a ratio of 3 : 1) in order to investigate the incorporated quantities of Fe–ZnO into the electrospun membranes.[53] It provided evidence to confirm the homogenous distribution of the incorporated nanohybrid throughout the electrospun cellulose acetate mat. As depicted in Fig. 5, Fig. 5f shows the places on the electrospun membrane

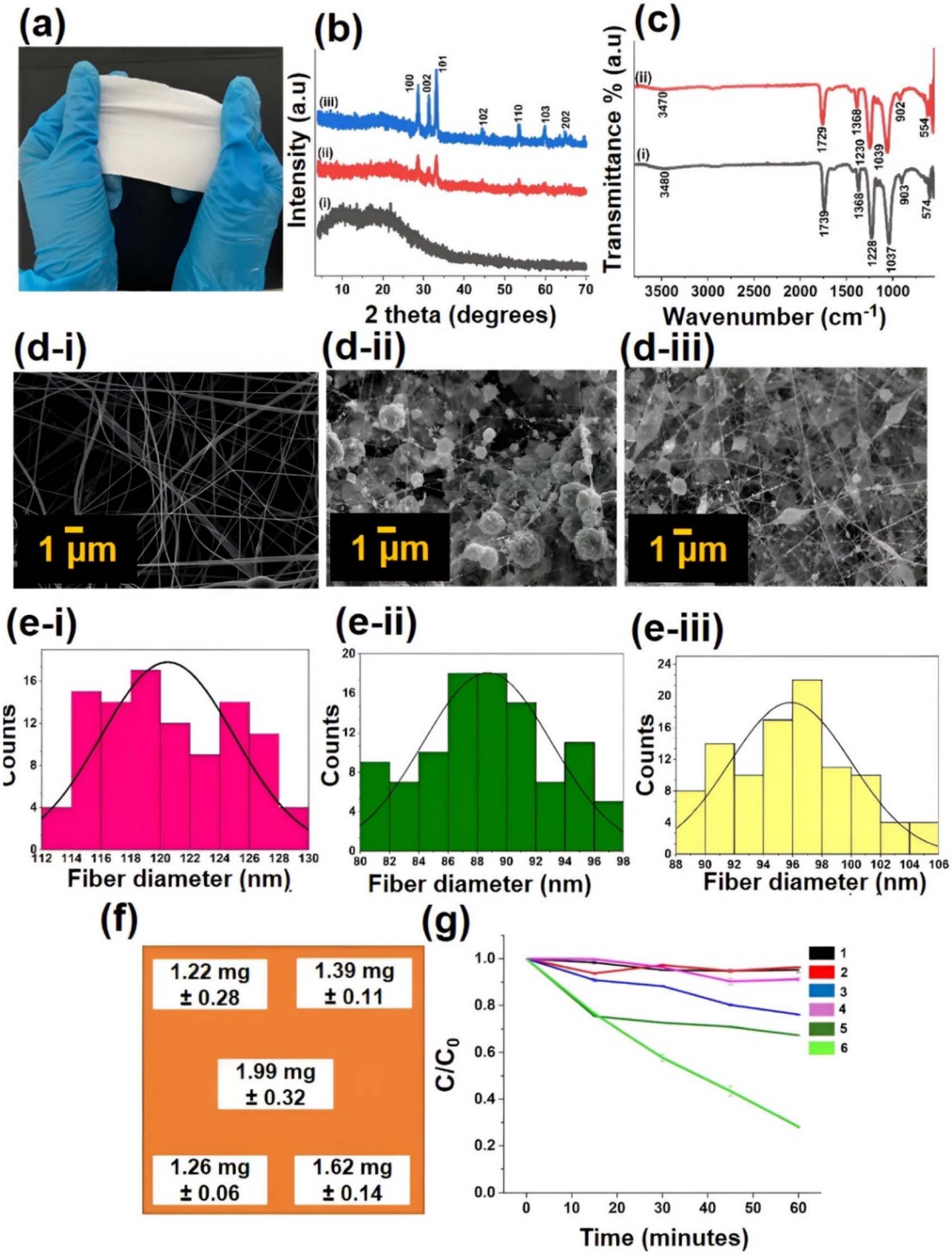

Fig. 5 (a) A photograph of the Fe 5%–ZnO incorporated electrospun membrane; (b) XRD spectra of nanofibers; (i) CA mat. (ii) ZnO incorporated CA mat, (iii) Fe 5%–ZnO incorporated CA mat; (c) FTIR spectra of nanofibers; (i) ZnO incorporated CA mat, (ii) Fe 5%–ZnO incorporated CA mat; (d) SEM images of; (i) CA mat, (ii) ZnO incorporated CA mat, (iii) Fe 5%–ZnO incorporated CA mat; (e) distribution of fiber diameter; (i) CA mat, (ii) ZnO incorporated CA mat and (iii) Fe 5%–ZnO incorporated CA mat; (f) content of Fe at each point in the electrospun CA membrane based on AAS results; (g) photocatalytic degradation of ZnO incorporated cellulose acetate fiber mat under, (1) Dark, (2) Lamp, (3) Normal light and Fe 5%–ZnO incorporated ZnO fiber mat under, (4) Dark, (5) Lamp and (6) Normal light.

where the samples were taken for acid digestion. Then each sample was analyzed by AAS analysis to investigate the quantity of Fe in the electrospun membrane. Fig. 5f depicts the mean value of Fe content at each point based on AAS results. It can be confirmed that the distribution of metal through the electrospun membrane is comparable in composition.

The degradation of MB dye by the Fe 5%–ZnO incorporated fiber mat was monitored through the reduction of characteristic absorption peak height (ESI Fig. S5†). Fig. 5g shows the photocatalytic degradation of ZnO incorporated cellulose acetate fiber mat and Fe 5%–ZnO incorporated ZnO fiber mat under dark, under visible light lamp, and under normal light. For 1 hour time period, Fe 5%–ZnO incorporated fiber mat kept under normal light showed highest degradation and it was found to be 72%. The degradation of ZnO fiber mat kept under normal light was found to be 24% and hence it can be determined that Fe 5%–ZnO fiber mat shows a promising photocatalytic activity compared to that undoped ZnO fiber mat. Under visible light lamp photocatalytic degradation of ZnO fiber mat and Fe 5%–ZnO fiber mat was found to be 16% and 34% respectively. For the samples kept under dark there was no distinguishable degradation found. Photocatalytic activity of Fe 5%–ZnO incorporated electrospun fiber mat shows significant improvement. It clearly indicates that the successful incorporation of Fe 5%–ZnO in the nanofiber mat can enhance the photocatalytic performance of fabricated fiber mats under visible light.[81]

The mechanochemical properties of cellulose acetate based electrospun membranes with nanomaterials were well studied by many researchers and they have already proven its suitability as a material with optimal mechanochemical properties for various applications.[82,83] Nauman *et al.* have described that various parameters including crystalline size and concentration of the incorporated material affect the mechanochemical properties of electrospun membranes.[84] Incorporation of metallic nanoparticles, organic molecules or crystalline structures into the electrospun membrane enhance the mechanical strength of the nanofiber mat as well as the thermal stability of the nanofiber mat.[85]

Aly *et al.* studied the mechanical properties of ZnO nanoparticles/graphene oxide (GO) cellulose acetate (CA) nanofibers and reported the tensile strength 5.44 ± 0.81, 12.87 ± 0.93, and 8.82 ± 1.2 MPa for ZnO@CA, GO@CA, and ZnO/GO@CA respectively. Further, toughness increased from 23.29 ± 1.4 MJ m^{-3}, to 68.95 ± 4.5, and 57.75 ± 3.6 MJ m^{-3} for ZnO@CA, GO@CA, and ZnO/GO@CA respectively[86] further, Ghosh *et al.* developed a zinc oxide cellulose acetate electrospun mats for efficient wound healing and reported that the reinforcement of ZnO into CA increased the tensile strength and young's modules of the nanofibrous scaffold with the increasement of ZnO concentration.[87]

3.6 Evaluation of radical scavenging activity of ZnO nanoparticles and Fe 5%–ZnO nanohybrid incorporated electrospun CA membranes by DPPH assay

As shown in Fig. 6a, the highest DPPH degradation value was shown by Fe 5%–ZnO nanohybrid incorporated CA fiber mat under normal light, and it was found to be 50.62%. Due to the lower band gap of Fe 5%–ZnO nanohybrid (Table 2), hydroxyl

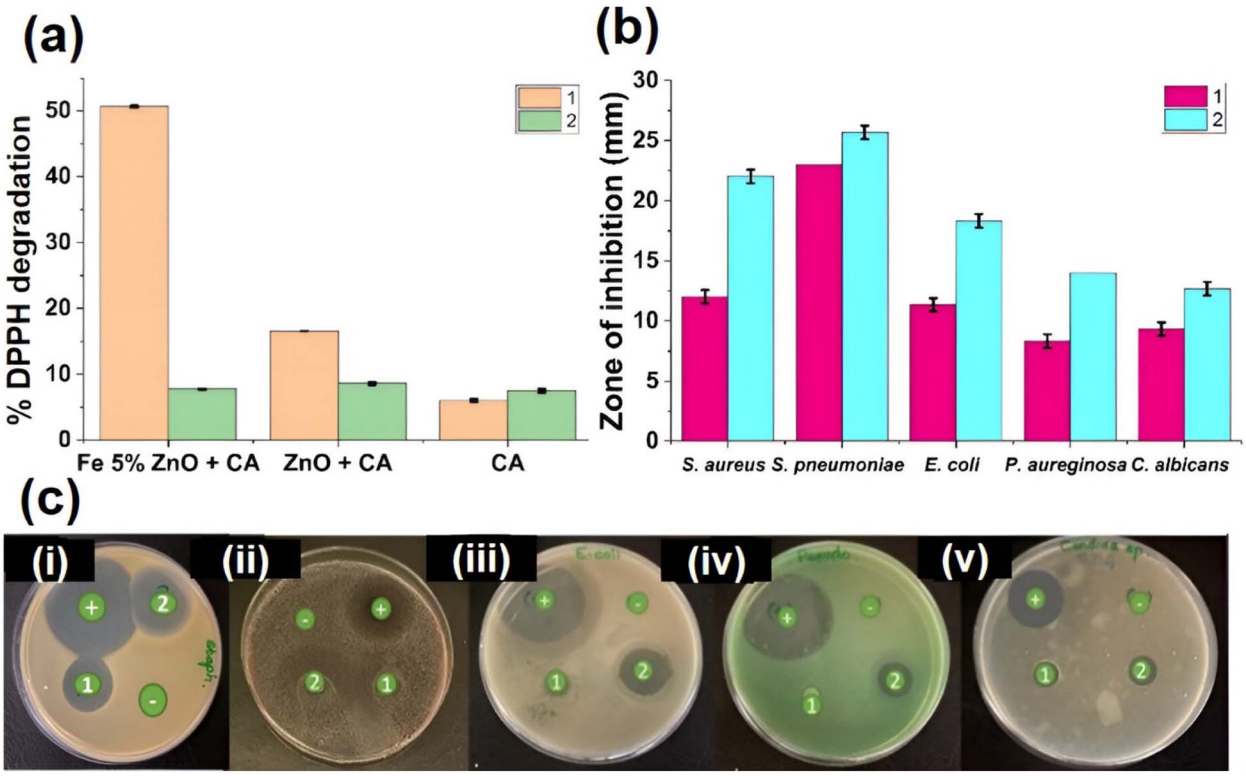

Fig. 6 (a) DPPH degradation percentage of Fe 5%–ZnO fiber mat, ZnO fiber mat and cellulose acetate fiber mat under normal light and dark; (1) normal light, (2) dark (b) zone of inhibition of disc diffusion test of ZnO fiber mat and Fe 5%–ZnO fiber mat using different microorganisms; (1) ZnO fiber mat, (2) Fe 5%–ZnO fiber mat (c) disc diffusion inhibition zones of; (i) *S. aureus* (ii) *S. pneumoniae* (iii) *E. coli* (iv) *P. aeruginosa* and (v) *C. albicans*; (+) positive control, (−) negative control, (1) ZnO incorporated CA mat and (2) Fe doped (5%) ZnO incorporated CA mat.

radical formation increased and as a result, the free radical scavenging activity of Fe 5%–ZnO nanohybrid showed the highest value. For ZnO incorporated cellulose acetate fiber mat, under normal light DPPH degradation was found to be 16.60%, and for cellulose acetate fiber mat, it was 6.01%.

These findings highlight the importance of radical scavenging activity in antimicrobial mechanisms of nanomaterials. The nanoparticles itself can be entered into the microbial cells and cause structural deformations and also physiological interruptions in the microbial cells. However, when it comes to the nanoparticles incorporated nanofiber mats, the nanoparticles remain within the nanofiber matrix. Electrospun CA membranes with a 25 cm^2 (5 cm × 5 cm) Fe 5%–ZnO nanohybrid were placed for 24 hours in bacterial cultures (cultured in nutrient broth agar) of *S. aureus* (Gram-positive bacteria), *E. coli* (Gram-negative bacteria) and fungal cultures (cultured in SDA broth agar) of *C. albicans* (fungi). The solutions were then subjected to IC-PMS analysis to assess metal leaching from electrospun membranes, however no such detections were made. Moreover, several studies have shown that there is no leaching out of nanoparticles from dense electrospun fibers.[82,83] According to Table 2, visible light governs the activation and initiation of ROS from metallic nanoparticles that give rise to antimicrobial potential, and these fabricated CA – mats have visible light active ROS generation, which governs their self-sterilizing ability. The radical scavenging activity is directly proportionate to the antimicrobial activity. Reactive oxygen species (ROS), which are generated by radical scavenging activity, suppress the antioxidant-dependent defense mechanism in microbial cells through lipid peroxidation and the oxidation of organelles, including proteins and DNA. Because most microorganisms generate an environment that is acidic in their host cells, catalysts dissolve in biological fluids as a result of this increased acidity.[88] The hydroxyl group synthesis in this phenomenon is then enhanced by the increased acidity.[86] This will cause the bacterial cells to run out of glutathione and produce more ROS, which have a variety of detrimental effects on the microbial cells.[89]

3.7 Evaluation of antimicrobial activity of ZnO nanoparticles and Fe 5%–ZnO nanohybrid incorporated electrospun CA membranes by disc diffusion method

According to the reported results, both electrospun membranes (ZnO incorporated membrane and Fe 5%–ZnO nanohybrid incorporated membrane) showed an antimicrobial activity against the tested microbes. The Fe 5%–ZnO nanohybrid incorporated electrospun membrane showed the best antimicrobial activity against the tested microbes. When analyzing the inhibition zones of the ZnO-incorporated electrospun mat, it also showed a comparative inhibition zone, but it was less than the Fe 5%–ZnO nanohybrid incorporated membrane. Fig. 6b depicted the zones of inhibition in a graph, and Fig. 6c depicted the graphical representation of zones of inhibition (disk diffusion) of each nanohybrid against all the tested microbes.

Furthermore, the Fe 5%–ZnO nanohybrid incorporated electrospun membrane showed greater antibacterial activity against the Gram-positive bacteria. This can be explained by the differences in the structure of the cell walls of Gram positive and Gram-negative bacteria. Gram-positive bacterial cell wall is simple, and it lacks the complex outer membrane. Whereas Gram-negative bacterial cell wall is complex and consist of four layers including the outer membrane containing lipopolysaccharides. Therefore, it is difficult to destroy the cell wall of Gram-negative bacteria. The minimum values of the inhibition zones among the tested bacteria were reported against *Pseudomonas aeruginosa*. It is considered a bacterium that is difficult to destroy because of its own antibacterial resistance mechanisms. The electrospun membranes showed promising antifungal activity as well. Fe–ZnO incorporated electrospun membranes showed a higher inhibition zone than ZnO incorporated electrospun membranes. Hence, the developed Fe 5%–ZnO nanohybrid incorporated electrospun membranes showed potential as an antimicrobial membrane that has both antibacterial and antifungal activity[90,91] under sunlight and normal light.

Considering the aforementioned data, it is well proven that metal-doped nanoparticles can be used as effective photocatalysts, and they can act as promising self-sterilizing materials under sunlight and normal light. However, it is always recommended to test clinical strains of the tested microorganism as well as few more pathogenic bacteria to confirm the above findings. The technique of electrospinning facilitates the embedding of these nanohybrids into a suitable polymer membrane. According to recent published literature, photocatalytic self-sterilization nanomaterials are a blooming discipline in nanotechnology and biomedicine. El-Moghazy and colleagues assessed the potent electrostatic interactions among anionic photosensitizers across a cationic nanosized cotton fiber surface in order to create photoinduced nano fabrics that, when exposed to radiation, generate reactive oxygen species (ROS) with a biocidal effect.[92] Moreover, the invention of water-repellent, TiO_2-organic dye-based air filters by Heo *et al.*, made it possible to photochemically inactivate bioaerosols in the presence of visible light.[93]

This research study will also fuse the interfaces of photocatalysis principles, nanotechnology, and microbiology in order to ensure that these photocatalytic nanohybrids incorporate electrospun membrane as an affordable, readily available, biocompatible, and effective self-sterilizing material for health care needs.[94–96]

4 Conclusion

In the present work, ZnO and Fe–ZnO nanohybrids were successfully synthesized *via* the co-precipitation method. The impact of varied Fe doping concentrations (0–10%) structural, morphological, compositional, optical, and antioxidant properties of ZnO nanostructure were studies and discussed. It is found from the PXRD data, that the crystalline parameters of the nanohybrids deteriorated with the increase in Fe doping concentration. This might be due to the substitution of Fe^{3+} ions into the Zn^{2+} ions in the ZnO lattice in all the doped samples. The SEM images exhibited a change in the morphology of ZnO from spherical nanoparticles to nanoflowers upon doping with Fe. The

FTIR investigation revealed the regular vibrational modes of Zn–O and Fe–O. AAS, and XPS analysis further confirmed the presence of Fe in the ZnO lattice. It is determined that the redshift of the band gap energy of ZnO upon doping Fe into the ZnO nanoparticles. In the photodegradation test, it was found that the Fe 5%–ZnO nanohybrid has the highest photocatalytic activity. DPPH IC_{50} assay studies were performed to evaluate the free radical scavenging capacities of ZnO and Fe 5%–ZnO nanohybrids. The incorporation of Fe 5%–ZnO nanohybrid into cellulose acetate polymer matrix by electrospinning was denoted by PXRD, FTIR, and SEM analysis. The higher loading of Fe 5%–ZnO nanohybrid into polymer such as 30% w/w showed prominent ZnO peaks in the PXRD pattern. The antimicrobial activity of prepared nanoparticles and nanofibers were evaluated under sunlight and normal light by disc diffusion and spread plate method, and it can be concluded that Fe 5%–ZnO nanofiber membranes can be used as a potential self-sterilizing material in healthcare settings.

Declaration

The authors have no relevant financial or non-financial interests to disclose.

Author contributions

K. Ranathunga and P. Yapa – conduct experiment, formal analysis of data and writing the manuscript. I.Munaweera – conceptualization, funding acquisition, methodology, supervision, writing, review and editing the original draft. C. Sandaruwan – software supervision, formal analysis of data, review and editing the original draft. M. Weerasekera – supervision, curation of microbiology data, review and editing the original draft.

Conflicts of interest

The authors declare that there is no conflict of interest.

Acknowledgements

Financial support for this study is acknowledged by the University of Sri Jayewardenepura, Sri Lanka under the research grant number ASP/01/RE/SCI/2022/15 and The World Academy of Science (20/102/RG/CHE/AS_1-FR3240314134) for providing grants for the electrospinning setup.

References

1 A. Haleem, M. Javaid, R. P. Singh, S. Rab and R. Suman, Applications of nanotechnology in medical field: a brief review, *J. Glob. Health*, 2023, (2), 70–77.
2 C. Madhusha, T. Jayasundara, I. Munaweera, C. Perera, G. Wijesinghe, M. Weerasekera, *et al.*, Synthesis and structural characterization of copper nanoparticles doped activated carbon derived from coconut coir for drinking water purification, *Mater. Today Chem.*, 2023, **27**(101312), 101312.
3 A. Kaushik, Biomedical Nanotechnology Related Grand Challenges and Perspectives, *Frontal Nanotechnol. Res.*, 2019, 1.
4 P. M. Armenante, and A. C. Kirpekar, Sterilization in the pharmaceutical and biotechnology industry, in *Handbook of Downstream Processing*, ed. E. Goldberg, Springer Netherlands, Dordrecht, 1997, pp. 261–308.
5 P. P. Fehér, Á. Madarász and A. Stirling, Prediction of Redox Power for Photocatalysts: Synergistic Combination of DFT and Machine Learning, *J. Chem. Theory Comput.*, 2023, **19**(13), 4125–4135.
6 Z. Zhang, A. Y. El-Moghazy, N. Wisuthiphaet, N. Nitin, D. Castillo, B. G. Murphy, *et al.*, Daylight-Induced Antibacterial and Antiviral Nanofibrous Membranes Containing Vitamin K Derivatives for Personal Protective Equipment, *ACS Appl. Mater. Interfaces*, 2020, **12**(44), 49416–49430.
7 Z. Edis, S. H. Bloukh, H. A. Sara and N. I. Azelee, Antimicrobial Biomaterial on Sutures, Bandages and Face Masks with Potential for Infection Control, *Polymers*, 2022, **14**(10), 1932.
8 S. Mohapatra, Sterilization and Disinfection, *Essentials of Neuroanesthesia*, Epub, 2017, pp. 929–944, DOI: **10.1016/B978-0-12-805299-0.00059-2**.
9 A. J. Jinia, N. B. Sunbul, C. A. Meert, C. A. Miller, S. D. Clarke, K. J. Kearfott, *et al.*, Review of Sterilization Techniques for Medical and Personal Protective Equipment Contaminated With SARS-CoV-2, *IEEE Access*, 2020, **8**, 111347–111354.
10 A. Ardeshna, K. Chavan, A. Prakasam, D. Ardeshna, D. Shah and K. Velliyagounder, Effectiveness of Different Sterilization Methods on Clinical Orthodontic Materials, *J. Indian Orthod. Soc.*, 2022, **57**(2), 98–105.
11 H. A. Foster, I. B. Ditta, S. Varghese and A. Steele, Photocatalytic disinfection using titanium dioxide: spectrum and mechanism of antimicrobial activity, *Appl. Microbiol. Biotechnol.*, 2011, **90**(6), 1847–1868.
12 K. Ouyang, K. Dai, S. L. Walker, Q. Huang, X. Yin and P. Cai, Efficient Photocatalytic Disinfection of Escherichia coli O157:H7 using C70-TiO2 Hybrid under Visible Light Irradiation, *Sci. Rep.*, 2016, **6**(1), 25702.
13 M. Y. Memar, R. Ghotaslou, M. Samiei and K. Adibkia, Antimicrobial use of reactive oxygen therapy: current insights, *Infect. Drug Resist.*, 2018, **11**, 567–576.
14 H. Li, X. Zhou, Y. Huang, B. Liao, L. Cheng and B. Ren, Reactive Oxygen Species in Pathogen Clearance: The Killing Mechanisms, the Adaption Response, and the Side Effects, *Front. Microbiol.*, 2021, **11**, 622534.
15 C. Weng, L. Shen, J. W. Teo, Z. C. Lim, B. S. Loh and W. H. Ang, Targeted Antibacterial Strategy Based on Reactive Oxygen Species Generated from Dioxygen Reduction Using an Organoruthenium Complex, *JACS Au*, 2021, **1**(9), 1348–1354.
16 B. M. M. Uddin, M. A. Yusuf and Z. A. Ratan, A Review of Superbug: A Global Threat in Health Care System, *Bangladesh J. Infect. Dis.*, 2018, **4**(1), 25–28.

17 S. N. Khan and A. U. Khan, Breaking the Spell: Combating Multidrug Resistant Superbugs, *Front. Microbiol.*, 2016, **7**, 174.
18 C. L. Ventola, The antibiotic resistance crisis: part 1: causes and threats. P & T: a peer-reviewed, *Bangladesh Journal of Infectious Diseases*, 2015, **40**(4), 277–283.
19 B. Felden and V. Cattoir, Bacterial Adaptation to Antibiotics through Regulatory RNAs, *Antimicrob. Agents Chemother.*, 2018, **62**(5), e02503.
20 S. Banerjee, K. Lo, N. Ojkic, R. Stephens, N. F. Scherer and A. R. Dinner, Mechanical feedback promotes bacterial adaptation to antibiotics, *Nat. Phys.*, 2021, **17**(3), 403–409.
21 R. Jadimurthy, S. Jagadish, S. C. Nayak, S. Kumar, C. D. Mohan and K. S. Rangappa, Phytochemicals as Invaluable Sources of Potent Antimicrobial Agents to Combat Antibiotic Resistance, *Life*, 2023, **13**(4), 948.
22 G. E. Yılmaz, I. Göktürk, M. Ovezova, F. Yılmaz, S. Kılıç and A. Denizli, Antimicrobial Nanomaterials: A Review, *Hygiene*, 2023, **3**(3), 269–290.
23 E. Sánchez-López, D. Gomes, G. Esteruelas, L. Bonilla, A. L. Lopez-Machado, R. Galindo, *et al.*, Metal-Based Nanoparticles as Antimicrobial Agents: An Overview, *Nanomaterials*, 2020, **10**(2), 292.
24 K. L. Seneviratne, I. Munaweera, S. E. Peiris, C. N. Peiris and N. Kottegoda, Recent Progress in Visible-Light Active (VLA) TiO2 Nano-Structures for Enhanced Photocatalytic Activity (PCA) and Antibacterial Properties: A Review, *Iran. J. Catal.*, 2021, 217–245.
25 P. Kodithuwakku, D. R. Jayasundara, I. Munaweera, R. Jayasinghe, T. Thoradeniya, M. Weerasekera, *et al.*, A review on recent developments in structural modification of TiO2 for food packaging applications, *Prog. Solid State Chem.*, 2022, **67**(100369), 100369.
26 I. Munaweera, and P. Yapa, *Principles and Applications of Nanotherapeutics*, CRC Press, 1st edn, 2024.
27 R. Y. K. Chang, S. C. Nang, H. K. Chan and J. Li, Novel antimicrobial agents for combating antibiotic-resistant bacteria, *Adv. Drug Delivery Rev.*, 2022, **187**, 114378.
28 I. Munaweera, and M. L. C. Madhusha, *Smart Nanomaterials*, CRC Press, 1st edn, 2023.
29 D. K. Sharma, S. Shukla, K. K. Sharma and V. Kumar, A review on ZnO: Fundamental properties and applications, *Mater. Today: Proc.*, 2022, **49**, 3028–3035.
30 K. Davis, R. Yarbrough, M. Froeschle, J. White and H. Rathnayake, Band gap engineered zinc oxide nanostructures *via* a sol–gel synthesis of solvent driven shape-controlled crystal growth, *RSC Adv.*, 2019, **9**(26), 14638–14648.
31 N. Kamarulzaman, M. F. Kasim and R. Rusdi, Band Gap Narrowing and Widening of ZnO Nanostructures and Doped Materials, *Nanoscale Res. Lett.*, 2015, **10**(1), 346.
32 N. M. Moussa, F. M. Ebrahim, K. Adly and M. Y. Hassaan, Chromium doped ZnO nanoparticles for energy storage, gas and humidity sensing and spin based electronic devices applications, *Opt. Quantum Electron.*, 2022, **54**(11), 683.
33 M. A. Ciciliati, M. F. Silva, D. M. Fernandes, M. A. C. de Melo, A. A. W. Hechenleitner and E. A. G. Pineda, Fe-doped ZnO nanoparticles: Synthesis by a modified sol–gel method and characterization, *Mater. Lett.*, 2015, **159**, 84–86.
34 S. A. Ahmed, Structural, optical, and magnetic properties of Mn-doped ZnO samples, *Results Phys.*, 2017, **7**, 604–610.
35 B. Yan, Y. Zhang, Z. Li, P. Zhou and Y. Mao, Electrospun nanofibrous membrane for biomedical application, *SN Appl. Sci.*, 2022, **4**(6), 172.
36 S. Meraz-Dávila, C. E. Pérez-García and A. A. Feregrino-Perez, Challenges and advantages of electrospun nanofibers in agriculture: a review, *Mater. Res. Express*, 2021, **8**(4), 042001.
37 S. Kumarage, I. Munaweera and N. Kottegoda, A comprehensive review on electrospun nanohybrid membranes for wastewater treatment, *Beilstein J. Nanotechnol.*, 2022, **13**, 137–159.
38 K. Qi, X. Xing, A. Zada, M. Li, Q. Wang, S.-y Liu, *et al.*, Transition metal doped ZnO nanoparticles with enhanced photocatalytic and antibacterial performances: Experimental and DFT studies, *Ceram. Int.*, 2020, **46**(2), 1494–1502.
39 B.-L. Guo, P. Han, L.-C. Guo, Y.-Q. Cao, A.-D. Li, J.-Z. Kong, *et al.*, The Antibacterial Activity of Ta-doped ZnO Nanoparticles, *Nanoscale Res. Lett.*, 2015, **10**(1), 336.
40 E. S. Permyakova, A. M. Manakhov, P. V. Kiryukhantsev-Korneev, D. V. Leybo, A. S. Konopatsky, Y. A. Makarets, *et al.*, Electrospun polycaprolactone/ZnO nanocomposite membranes with high antipathogen activity, *Polymers*, 2022, **14**(24), 5364.
41 A. D. Sekar, V. Kumar, H. Muthukumar, P. Gopinath and M. Matheswaran, Electrospinning of Fe-doped ZnO nanoparticles incorporated polyvinyl alcohol nanofibers for its antibacterial treatment and cytotoxic studies, *Eur. Polym. J.*, 2019, **118**, 27–35.
42 S. Rajan, A. Venugopal, H. Kozhikkalathil, S. Valappil, M. Kale, M. Mann, *et al.*, Synthesis of ZnO nanoparticles by precipitation method: Characterizations and applications in decipherment of latent fingerprints, *Mater. Today: Proc.*, 2023, DOI: **10.1016/j.matpr.2023.05.680**.
43 M. Musharaf, S. Karamat, U. Hassan, U. Khalique, A. Oral, A. Behjat, *et al.*, Solubility Enhancement of Fe in ZnO Nanoparticles Prepared by Co-Precipitation Method, *J. Supercond. Novel Magn.*, 2021, **34**, 2633–2642.
44 S. Bharanidharan, K. Sathiyamurthy and B. Sheeba, Using Co-Precipitation Method Determining Synthesis and Characterization of Fe Doped Zinc Oxide Nanoparticles, *Int. J. Innovative Technol. Explor. Eng.*, 2019, **8**, 705–707.
45 I. Munaweera, and M. L. C. Madhusha, *Characterization Techniques for Nanomaterials*, CRC Press, 1st edn, 2023.
46 H. Sutanto, I. Alkian, M. Mukholit, A. A. Nugraha, E. Hidayanto, I. Marhaendrajaya, *et al.*, Analysis of Fe-doped ZnO thin films for degradation of rhodamine b, methylene blue, and Escherichia coli under visible light, *Mater. Res. Express*, 2021, **8**(11), 116402.
47 E. Şahin, S. J. Musevi and A. Aslani, Antibacterial activity against Escherichia coli and characterization of ZnO and

ZnO–Al2O3 mixed oxide nanoparticles, *Arabian J. Chem.*, 2017, **10**, S230–S235.

48 I. Ahmad, M. Y. Alshahrani, S. Wahab, A. I. Al-Harbi, N. Nisar, Y. Alraey, *et al.*, Zinc oxide nanoparticle: An effective antibacterial agent against pathogenic bacterial isolates, *J. King Saud Univ., Sci.*, 2022, **34**(5), 102110.

49 B. Abebe, E. A. Zereffa, A. Tadesse and H. C. A. Murthy, A Review on Enhancing the Antibacterial Activity of ZnO: Mechanisms and Microscopic Investigation, *Nanoscale Res. Lett.*, 2020, **15**(1), 190.

50 B. B. de Menezes, L. M. Frescura, R. Duarte, M. A. Villetti and M. B. da Rosa, A critical examination of the DPPH method: Mistakes and inconsistencies in stoichiometry and IC50 determination by UV–Vis spectroscopy, *Anal. Chim. Acta*, 2021, **1157**, 338398.

51 J. Jumina, D. Siswanta, K. Zulkarnain, S. Triono, P. Priatmoko, E. Yuanita, *et al.*, Development of C-Arylcalix resorcinarenes and C-Arylcalix[4]pyrogallolarenes as Antioxidant and UV-B Protector, *Indones. J. Chem.*, 2019, **19**, 273.

52 S. Kumarage, I. Munaweera, C. Sandaruwan, L. Weerasinghe and N. Kottegoda, Electrospun amine-functionalized silica nanoparticles - cellulose acetate nanofiber membranes for effective removal of hardness and heavy metals (As(V), Cd(II),Pb(II)) in drinking water sources, *Environ. Sci.: Water Res. Technol.*, 2023, **9**, 2664–2679.

53 A. B. M. H. Uddin, R. S. Khalid, M. Alaama, A. M. Abdualkader, A. Kasmuri and S. A. Abbas, Comparative study of three digestion methods for elemental analysis in traditional medicine products using atomic absorption spectrometry, *J. Anal. Sci. Technol.*, 2016, **7**(1), 6.

54 Z. Kalaycıoğlu, B. Özuğur Uysal, Ö. Pekcan and F. B. Erim, Efficient Photocatalytic Degradation of Methylene Blue Dye from Aqueous Solution with Cerium Oxide Nanoparticles and Graphene Oxide-Doped Polyacrylamide, *ACS Omega*, 2023, **8**(14), 13004–13015.

55 P. N. Yapa, I. Munaweera, C. Sandaruwan, L. Weerasinghe and M. M. Weerasekera, Metal doped silica nanohybrids with extensive bacterial coverage for antibacterial applications exhibit synergistic activity, *Biomater. Adv.*, 2024, **157**, 213753.

56 S. E. Peiris, K. L. Seneviratne, R. P. A. Shashikala, C. N. Peiris, M. I. Imalka, and Y. P. Piumika, In vitro evaluation of antibacterial activity of copper and sulfur nanoparticles for controlling bacterial blight caused by Xanthomonas sp. in *Anthurium Andraeanum Lind*, SLIIT J Hum & Sci, 2022, vol. 3, (1), pp. 46–55.

57 Clsi.org., cited 2024 Mar 6, available from,**https://clsi.org/media/osthhxax/m27m44sed3e_sample.pdf**.

58 N. B. Mahmood, F. R. Saeed, K. R. Gbashi and U.-S. Mahmood, Synthesis and characterization of zinc oxide nanoparticles *via* oxalate co-precipitation method, *Mater. Lett.: X*, 2022, **13**, 100126.

59 R. E. Adam, G. Pozina, M. Willander and O. Nur, Synthesis of ZnO nanoparticles by co-precipitation method for solar driven photodegradation of Congo red dye at different pH, *Photonics Nanostructures: Fundam. Appl.*, 2018, **32**, 11–18.

60 K. Nagarajan, B. Kataru, N. Sravani, T. Vigneshwari, A. Panneerselvam and D. Rajeswari, Biosynthesis of Zinc oxide nanoparticles using culture filtrates of Aspergillus niger: Antimicrobial textiles and dye degradation studies, *OpenNano*, 2018, **3**, 48–55.

61 M. Pal, U. Pal, J. M. G. Y. Jiménez and F. Pérez-Rodríguez, Effects of crystallization and dopant concentration on the emission behavior of TiO2:Eu nanophosphors, *Nanoscale Res. Lett.*, 2012, **7**(1), DOI: **10.1186/1556-276x-7-1**.

62 N. Jayarambabu, Germination and Growth Characteristics of Mungbean Seeds (Vigna radiata L.) affected by Synthesized Zinc Oxide Nanoparticles, *Int. J. Curr. Eng. Technol.*, 2014, **4**, 5.

63 K. Raja, P. S. Ramesh and D. Geetha, Structural, FTIR and photoluminescence studies of Fe doped ZnO nanopowder by co-precipitation method, *Spectrochim. Acta, Part A*, 2014, **131**, 183–188.

64 R. Al-Gaashani, S. Radiman, A. R. Daud, N. Tabet and Y. Al-Douri, XPS and optical studies of different morphologies of ZnO nanostructures prepared by microwave methods, *Ceram. Int.*, 2013, **39**(3), 2283–2292.

65 A. Popa, O. Pana, M. Stefan, D. Toloman, M. Stan, C. Leostean, *et al.*, Interplay between ferromagnetism and photocatalytic activity generated by Fe3+ ions in iron doped ZnO nanoparticles grown on MWCNTs, *Phys. E*, 2020, **129**, 114581.

66 M. Karavasilis, M. Theodoropoulou and C. Tsakiroglou, A comparative study of the performance of zinc oxide and iron oxide doped-zinc oxide photocatalysts toward the oxidization of phenol under UV-radiation and sunlight, *IOP Conf. Ser. Earth Environ. Sci.*, 2021, **899**, 012069.

67 M. Carofiglio, M. Laurenti, V. Vighetto, L. Racca, S. Barui, N. Garino, *et al.*, Iron-Doped ZnO Nanoparticles as Multifunctional Nanoplatforms for Theranostics, *Nanomaterials*, 2021, **11**(10), 2628.

68 C. P. Rajan, N. Abharana, S. N. Jha, D. Bhattacharyya and T. T. John, Local Structural Studies Through EXAFS and Effect of Fe2+or Fe3+ Existence in ZnO Nanoparticles, *J. Phys. Chem. C*, 2021, **125**(24), 13523–13533.

69 S. Sathyanathan, S. Karthikeyan and K. Jayamoorthy, Spectral investigations to the effect of bulk and nano ZnO on peanut plant leaves, *Karbala Int. J. Mod. Sci.*, 2016, **2**, 69–77.

70 A. Durairaj, S. Nilavazhagan, A. Santhanam, N. Chidhambaram, G. Kanimozhi, T. Ahamad, *et al.*, The effect of iron doping on the structural, optical, surface morphological, and temperature-dependent magnetic properties of ZnO nanoparticles, *J. Phys.: Condens. Matter*, 2020, **33**, 094001.

71 S. C. S. Lemos, T. KdL. Rezende, M. Assis, FdC. Romeiro, D. A. Peixoto, EdO. Gomes, *et al.*, Efficient Ni and Fe doping process in ZnO with enhanced photocatalytic activity: A theoretical and experimental investigation, *Mater. Res. Bull.*, 2022, **152**, 111849.

72 C. A. Marin-Flores, O. Rodríguez-Nava, M. García-Hernández, R. Ruiz-Guerrero, F. Juárez-López and AdJ. Morales-Ramírez, Free-radical scavenging activity properties of ZnO sub-micron particles: size effect and kinetics, *J. Mater. Res. Technol.*, 2021, **13**, 1665–1675.

73 Y. K. Mohanta, S. K. Panda, R. Jayabalan, N. Sharma, A. K. Bastia and T. K. Mohanta, Antimicrobial, Antioxidant and Cytotoxic Activity of Silver Nanoparticles Synthesized by Leaf Extract of Erythrina suberosa (Roxb.), *Front. Mol. Biosci.*, 2017, **4**, DOI: **10.3389/fmolb.2017.00014**.

74 W. S. Koe, J. W. Lee, W. C. Chong, Y. L. Pang and L. C. Sim, An overview of photocatalytic degradation: photocatalysts, mechanisms, and development of photocatalytic membrane, *Environ. Sci. Pollut. Res. Int.*, 2020, **27**(3), 2522–2565.

75 R. Ameta, M. S. Solanki, S. Benjamin, and S. C. Ameta, Photocatalysis, in *Advanced Oxidation Processes for Waste Water Treatment*, Elsevier, 2018, pp. 135–75, DOI: **10.1016/B978-0-12-810499-6.00006-1**.

76 Z. Yu, Q. Li, J. Wang, Y. Yu, Y. Wang and Q. Zhou, Reactive Oxygen Species-Related Nanoparticle Toxicity in the Biomedical Field, *Nanoscale Res. Lett.*, 2020, **15**(1), 115.

77 I. Munaweera, and P. Yapa, *Principles and Applications of Nanotherapeutics*, CRC Press, Boca Raton, 2024.

78 S. Suryani, A. Damayanti, H. Heryanto, R. Rahmat, S. Syarifuddin and D. Tahir, High efficiency self-cleaning of nanocomposites ZnO with additional chitosan for helping electron and hole transport, *Int. J. Biol. Macromol.*, 2023, **224**, 125–132.

79 K. Ravichandran, R. Rathi, M. Baneto, K. Karthika, P. Rajkumar, B. Sakthivel, *et al.*, Effect of Fe+F doping on the antibacterial activity of ZnO powder, *Ceram. Int.*, 2015, **41**, 3390–3395.

80 C. Voorhis, J. Gonzalez-Benito and A. Kramar, "Nano in Nano"—Incorporation of ZnO Nanoparticles into Cellulose Acetate–Poly(Ethylene Oxide) Composite Nanofibers Using Solution Blow Spinning, *Polymers*, 2024, **16**, 341.

81 J. Qin, X. Zhang, C. Yang, M. Cao, M. Ma and R. Liu, ZnO microspheres-reduced graphene oxide nanocomposite for photocatalytic degradation of methylene blue dye, *Appl. Surf. Sci.*, 2017, **392**, 196–203.

82 R. Borges, L. F. M. Amaral, T. J. Bondancia, R. A. de Freitas, F. Wypych and C. Ribeiro, Mechanochemical conversion of cellulose acetate from residues to cellulosic nanospheres for emulsion application, *J. Environ. Chem. Eng.*, 2023, **11**(3), 110119.

83 P. Shukla, A. K. Bajpai and R. Bajpai, Structural, morphological, thermal and mechanical characterization of cellulose acetate–poly (acrylonitrile) semi interpenetrating polymer network (IPN) membranes and study of their swelling behavior, *Polym. Bull.*, 2016, **73**(8), 2245–2264.

84 S. Nauman, G. Lubineau and H. F. Alharbi, Post processing strategies for the enhancement of mechanical properties of ENMs (electrospun nanofibrous membranes): A review, *Membranes*, 2021, **11**(1), 39.

85 Z. Hao, J. Wu, C. Wang and J. Liu, Electrospun polyimide/metal-organic framework nanofibrous membrane with superior thermal stability for efficient PM2.5 capture, *ACS Appl. Mater. Interfaces*, 2019, **11**(12), 11904–11909.

86 A. A. Aly and M. K. Ahmed, Nanofibers of cellulose acetate containing ZnO nanoparticles/graphene oxide for wound healing applications, *Int. J. Pharm.*, 2021, **598**(120325), 120325.

87 S. Ghosh, S. Vaidya, N. More, R. Velyutham and G. Kapusetti, Piezoelectric-based bioactive zinc oxide-cellulose acetate electrospun mats for efficient wound healing: an *in vitro* insight, *Front. Immunol.*, 2023, **14**, 1245343.

88 Z. Yu, Q. Li, J. Wang, Y. Yu, Y. Wang and Q. Zhou, Reactive Oxygen Species-Related Nanoparticle Toxicity in the Biomedical Field, *Nanoscale Res. Lett.*, 2020, **15**(1), 115.

89 S. Ghosh, S. Vaidya, N. More, R. Velyutham and G. Kapusetti, Piezoelectric-based bioactive zinc oxide-cellulose acetate electrospun mats for efficient wound healing: an *in vitro* insight, *Front. Immunol.*, 2023, **14**, 1245343.

90 D. Kossyvaki, M. Bustreo, M. Contardi, A. Athanassiou and D. Fragouli, Functional Polymeric Membranes with Antioxidant Properties for the Colorimetric Detection of Amines, *Sensors*, 2023, **23**(22), 9288.

91 S. Park, H. Lee, S.-H. Shin, N. Kim, D. Shin and B. Bae, Increasing the Durability of Polymer Electrolyte Membranes Using Organic Additives, *ACS Omega*, 2018, **3**(9), 11262–11269.

92 A. El-Moghazy, *Daylight-Induced Antibacterial and Antiviral Cotton Cloth for Offensive Personal Protection*, 2020.

93 K. J. Heo and S. B. Jeong, Water-Repellent TiO(2)-Organic Dye-Based Air Filters for Efficient Visible-Light-Activated Photochemical Inactivation against Bioaerosols, *Nano Lett.*, 2021, **21**(4), 1576–1583.

94 X. Zhu, C. Xu, M. Jie, Y. Zhang and Y. Bai, Protonated carbon nitride for rapid photocatalytic sterilization *via* synergistic oxidative damage and physical destruction, *J. Environ. Sci.*, 2025, **149**, 188–199.

95 A. D. S. Montallana and M. R. Vasquez, Fabrication of PVA/Ag-TiO2 nanofiber mats for visible-light-active photocatalysis, *Results Phys.*, 2021, **25**, 104205.

96 I. P. Madhushika, P. Yapa, I. Munaweera, C. Sandaruwan and M. M. Weerasekera, The antimicrobial synergy of polymer based nanofiber mats reinforced with antioxidants intercalated layered double hydroxides as a potential active packaging material, *Nano Express*, 2024, **5**(2), 025018.